Correspondence to:
J. A. Carter,
jac48@le.ac.uk

Mean Energy Flux, Associated Derived Height-Integrated Conductances, and Field-Aligned Current Magnitudes Evolve Differently During a Substorm

J. A. Carter[1] [iD], **S. E. Milan[1]** [iD], **C. Forsyth[2]** [iD], **M. E. Lester[1]** [iD], **M.-T. Walach[3]** [iD], **J. Gjerloev[4]** [iD], **L. J. Paxton[4]** [iD], and **B. J. Anderson[4]** [iD]

[1]School of Physics and Astronomy, University of Leicester, University Road, Leicester, UK, [2]UCL Mullard Space Science Laboratory, Dorking, UK, [3]Physics Department, Lancaster University, Bailrigg, UK, [4]Applied Physics Laboratory, John Hopkins University, Laurel, MD, USA

Abstract We examine the average evolution of precipitation-induced height-integrated conductances, along with field-aligned currents (FACs), in the nightside sector of the polar cap over the course of a substorm. Conductances are estimated from the average energy flux and mean energies derived from auroral emission data. Data are binned using a superposed epoch analysis on a normalized time grid based on the time between onset and recovery phase (δt) of each contributing substorm. We also examine conductances using a fixed time binning of width 0.25 hr. We split the data set by magnetic latitude of onset. We find that the highest conductances are observed for substorms with onsets that occur between 63 and 65° magnetic latitude, peaking at around 11 mho (Hall) and 4.8 mho (Pedersen). Substorms with onsets at higher magnetic latitudes show lower conductances and less variability. Changes in conductance over the course of a substorm appear primarily driven by changes (about 40% at onset) in the average energy flux, rather than the average energy of the precipitation. Average energies increase after onset slower than energy flux, later these energies decrease slowly for the lowest latitude onsets. No clear expansion of the main region 1 and region 2 FACs is observed. However, we do see an ordering of the current magnitudes with magnetic latitude of onset, particularly for region 1 downwards FAC in the morning sector. Peak current magnitudes occur slightly after or before the start of the recovery phase for the normalized and fixed-time grids.

Plain Language Summary Particles precipitate from Earth's magnetosphere into the upper ionosphere causing auroral emissions. A comparison of these auroral emissions, taken at different wavelengths, can be used to estimate the mean energy of the particles, as well as the flux, or number of precipitating particles in an area per unit time. From this mean energy and flux, we can estimate changes in the conductance of the ionosphere. Here, we examine how the conductance varies during the course of a substorm; when increased auroral emissions are seen suddenly on the nightside of the Earth. For this work we use imaging data from low-altitude spacecraft that give reasonable spatial coverage of the nightside ionosphere. We compare the changes in conductance over the course of an average substorm, to those seen in electrical currents that flow in the Earth's magnetosphere. The currents respond in a similar manner to the parameters derived from the auroral emissions.

1. Introduction

Deciphering the spatial and temporal variations in ionospheric conductances, under a variety of ambient conditions is of importance to the solar-terrestrial community (Denton et al., 2016). Knowledge of the conductance, is of particular importance, for example, when considering the coupling of component regions within magnetosphere and the thermosphere. Auroral imagers offer a method to estimate height-integrated conductances induced through particle precipitation simultaneously over large areas of the high-latitude polar cap region (Lam et al., 2019). There may be considerable differences between spatially precise, height-resolved conductances, and those presented in statistical maps (McGranaghan et al., 2015). However, statistical maps still have value as primers for global magnetospheric-ionospheric coupling models, particularly under extreme conditions (Mukhopadhyay et al., 2020). Parameterization of height-integrated conductances at the dayside, under varying interplanetary magnetic field (IMF) and solar wind conditions, along with a simple parameterization during an average substorm on the nightside, was presented in Carter et al. (2020). In this previous work, only the substorm

phase relative to onset time was considered, using a superposed epoch analysis based on substorm onsets determined from the SuperMAG data set (Gjerloev, 2012; Newell & Gjerloev, 2011). In this work we parameterize height-integrated conductances by substorm phase and also by the magnetic latitude of substorm onset, as this is known to control substorm intensity (Milan et al., 2009). We also consider the evolution of these conductances with respect to distributions of field-aligned currents (FACs), which are an integral component of the magnetosphere-ionosphere coupled system.

Lester et al. (1996) examined Hall and Pedersen conductances during an individual substorm using an incoherent scatter radar. They found that the implied mean energy of the incoming precipitation varied during the progression of the substorm, which involved two expansion phases. At onset, the conductances were seen to increase to exceptionally high values of approximately 77 mho and 26 mho for Hall and Pedersen conductances respectively, whereas the mean energy remained constant. The second expansion phase showed a marked increase in mean energy, which was then doubled during the recovery phase. The authors suggested that the variations in mean energy were due to changes in acceleration processes in the magnetotail during the phase of a substorm, although observational effects from the radar are not discounted.

FACs in the Earth's magnetosphere respond to the substorm cycle in a variety of ways. The main region 1 and region 2 FAC distributions expand quickly to lower latitudes in the growth phase, and simultaneously increases are seen in both region 1 and region 2 current magnitudes, although the increase is larger for region 1 (Coxon et al., 2014). The FAC latitude and magnitudes recover within about 20 min. Asymmetries in the response of the FACs at onset are observed associated with the sign of the IMF B_Y component (Milan et al., 2018). (Olifer et al., 2021) examined heigh-integrated Pedersen conductances with respect to during substorms derived from low-altitude measurements of magnetic and electric fields. They found dawn-dusk asymmetries, whereby conductances associated with upwards, region 2 FACs exceeded those of the downwards, region 1 FACs in the dawn sector, by approximately 0.6 S. This discrepancy between upwards and downwards currents was not observed in the dusk sector. The authors attributed this difference to electron injections from the magnetotail during substorm breakup, occurring predominantly in the dawn sector.

This paper is laid out as follows. In Section 2 we describe the data sets used to derive Pedersen and Hall height-integrated conductance values from observations of auroral emissions, FACs, and the substorm list on which we based our superposed epoch analysis. Here we also describe both a substorm-expansion phase binning and a fixed-time binning used for the superposed epoch analysis. We compare distributions of mean energy, mean energy flux, and the derived Pedersen and Hall height-integrated conductances in relation to the FACs during the progress of an average substorm in Section 3, which we then discuss in Section 4. We conclude in Section 5.

2. Data

We use a superposed epoch analysis of substorm phase to parameterize the other datasets described below. This study uses a modified Substorm Onsets and Phases from Indices of the Electrojet (SOPHIE) list from Forsyth et al. (2015) which had been constructed using SML indices from the SuperMAG data (Gjerloev, 2012), and covers the years 2005 until 2019. The SOPHIE technique creates lists of substorms based on the rate of change of SML exceeding some percentile of the observed rates of change. (Forsyth et al., 2015) showed that, of the three percentiles examined (50th, 75th, and 90th), events based on the 75th percentile gave similar results to other substorm lists. As such, we use a list based on this percentile in this study. The SOPHIE event list contains the start of the expansion and recovery phases, and has been modified to now include the MLT and magnetic latitude of the SuperMAG station providing the SML index at the start of each phase. We take the start of the expansion phase as the onset time. For this analysis, we only include substorm onsets that occurred between 18hr MLT and 06hr MLT, which we parameterize by onset latitude. We only used isolated substorms, that is, those onsets that were preceded by a growth phase and followed by a recovery phase. This is to avoid multiple intensifications without an interim recovery period, and although these occur rarely (1% of time) (Milan et al., 2021), their effects could be large. The onset latitude bin boundaries were chosen to give good coverage of at least several hundreds of onsets per bin for the statistical analysis, with bins with a width of 2° starting from 63°, apart from the bins at the extremes of the range. As in the study of Carter et al. (2020), substorm phases are taken at set intervals before and after onset. We define δt as the time period between onset and the start of the recovery phase for each contributing substorm. The expansion and recovery phase starts are given in the supplementary material of Forsyth et al. (2015). The duration of each substorm is not defined in this list. We use a step size of 0.25 δt over
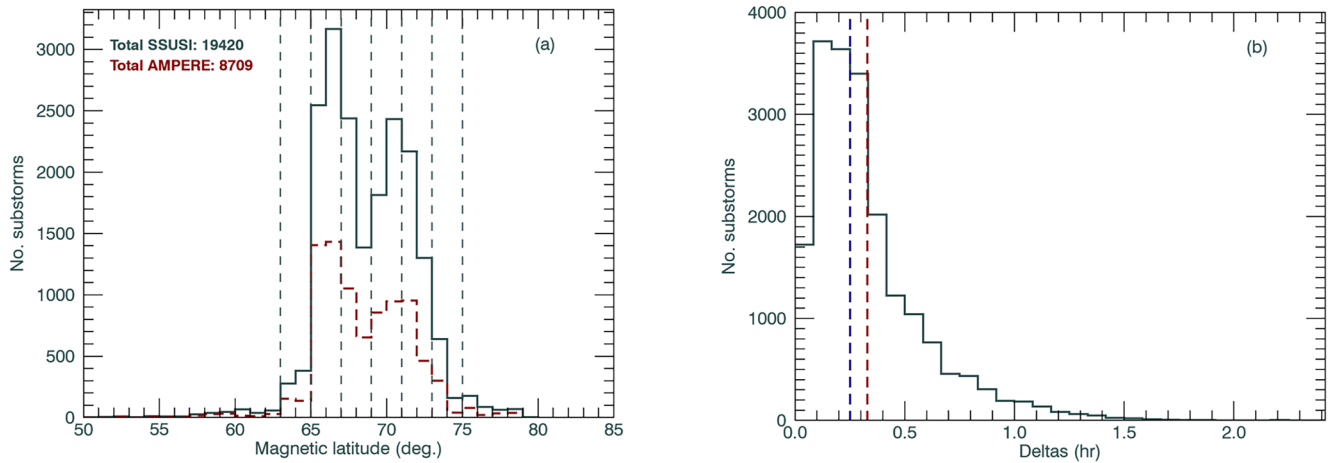
Figure 1. Statistics of the substorm onsets used in this analysis. Plot (a) A histogram of substorm onset latitudes from the (Forsyth et al., 2015) during the Special Sensor Ultraviolet Spectrographic Imager (gray) and the shorter, but superimposed AMPERE (red) data periods. Dashed vertical lines indicate the boundaries used for the latitude selection in this analysis. Plot (b) A histogram of all δt, defined as the interval between the start of the substorm expansion and recovery phase (E–R) from the (Forsyth et al., 2015) list. The mean and median δt values are marked by the red and blue vertical dashed lines, respectively.

the course of a substorm in our analysis below. We also examine the behavior over an average substorm by using a time bin of a fixed width of 0.25 hr.

In Figure 1 we plot a histogram of substorm onset latitudes used in this study, along with a histogram of the δt intervals. Histograms for onset magnetic latitudes occurring during both the Special Sensor Ultraviolet Spectrographic Imager (SSUSI) (gray line) and AMPERE (red dashed line) data ranges are shown in plot (a), and a histogram of δt is shown in plot (b). The mean δt value is 0.32 hr, or 19.8 min. The minimum δt used in this analysis was 2 min.

Later in this paper we present Pedersen and Hall height-integrated conductances derived from auroral emissions data obtained by the SSUSI (Paxton & Anderson, 1992; Paxton & Zhang, 2016) on board three Defense Meteorological Satellite Programme (DMSP) spacecraft. We calculate the conductances from data products produced by the SSUSI team, and we describe these calculations and data products fully in Carter et al. (2020). However in summary, the conductances are calculated from the mean energy and mean energy flux of the incoming precipitating particles, which are assumed to be electrons, derived from Lyman-Birge-Hopfield (LBH) long (165–180 nm) and short band (140–150 nm) radiances. We use SSUSI data from the Southern Hemisphere in this paper, as we have good coverage of the midnight local time sectors for all three DMSP spacecraft. The data originates from all available SSUSI files in the time period from 1 January 2005 to 31 December 2016 for F16, from 11 December 2006 to 4 August 2017 for F17, and from 17 November 2009 to 31 December 2017 for F18.

The calculation proceeded as follows. From the mean energy (E_0, in units of keV) and mean energy flux (Q, in units of erg cm^{-2} s^{-1}), the height-integrated Pedersen (Σ_P) and Hall (Σ_H) conductances can be calculated per pixel, via the empirical expressions found in Robinson et al. (1987), and as shown in Equations 1 and 2.

$$\Sigma_P = \frac{40E_0}{16 + E_0^2}\sqrt{Q} \tag{1}$$

$$\Sigma_H = 0.45\left(E_0^{0.85}\right)\Sigma_P \tag{2}$$

The Robinson et al. (1987) formula for height-integrated conductance is widely used in the community, although with significant limitations (Liemohn, 2020). There are alternative calculations and models for conductance, for example, the GLobal AirglOW model (McGranaghan et al., 2015). This study presents conductances calculated from the mean energy and mean energy flux of precipitating electrons, as derived from auroral emissions at two wavelengths. A larger study, comparing conductances calculated by a selection of methods, may form the basis of a future study.

To make a set of conductance maps, at each UT-stamped pixel at a given projected magnetic local time and magnetic latitude, the value of E_0 and Q are considered separately from each contributing DMSP satellite, and
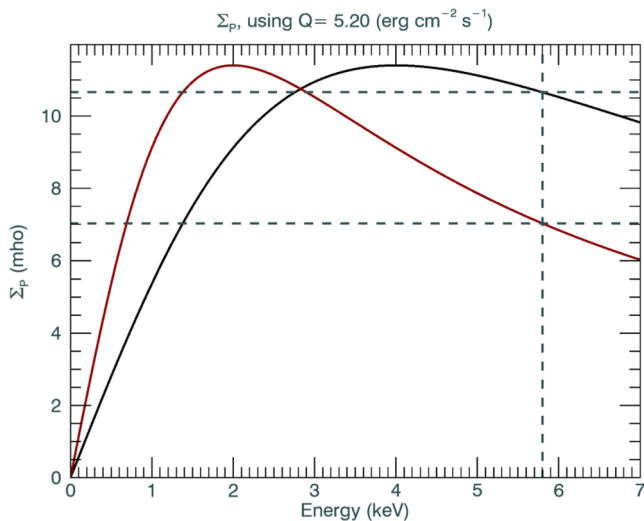
Figure 2. Height-integrated Pedersen conductances calculated using Equation 1 by assumed characteristic energy of the incoming particle precipitation, using the average mean energy flux of the Special Sensor Ultraviolet Spectrographic Imager (SSUSI) data set used in this work. This is calculated for a Maxwellian (red) or Gaussian (gray) distribution. Dashed lines indicate the average mean energy of the SSUSI data set.

used to calculate the Hall and Pedersen height-integrated conductances for that particular pixel. The conductances are then averaged at a given pixel to provide a series of images showing the average nightside spatial distribution of conductance at each substorm time step, whether fixed or related to δt, and for each latitude bin.

In this work we use SSUSI data products of mean energy and mean energy flux. These have been calculated based on the assumption of a Gaussian profile for the incoming particle precipitation energy distribution. Maxwellian and Gaussian distributions will have the same characteristic energy, but different mean energies (Robinson et al., 1987). Applying Equation 1 to an average energy flux of 5.2 erg cm^{-2} s^{-1} and an average mean energy of 5.8 keV over the entire SSUSI data set used in this work, the Gaussian assumption would overestimate the height-integrated conductance at 10.7 mho compared to 7.0 mho for a Maxwellian distribution, see Figure 2. Parity between distributions occurs for a characteristic energy of 2.85 keV, below which the Maxwellian assumption would overestimate the height-integrated conductance as compared to the Gaussian assumption. We present the calculated conductances as well as the behavior of E_0 and Q in Section 3.

The auroral-derived products are accompanied by patterns of FACs, obtained from the Active Magnetosphere and Planetary Electrodynamics Response Experiment (AMPERE) (Anderson et al., 2000; Waters et al., 2001). The FACs have been organized with respect to substorm latitude and substorm phase in the same way as the spatial distributions of E_0, Q, and conductance as described above. Contributing AMPERE data spans the period 1 January 2010 to 31 December 2016, which was available at the time of processing. Only current densities over 0.1 μA m^{-2} are included to avoid including spurious low current density values that result from the AMPERE data processing technique, similar to the threshold used in Clausen et al. (2012) at the level of a two sigma detection above the background as shown in Anderson et al. (2014).

3. Results

In Figure 3, we plot an example series of images showing the nightside spatial distribution of height-integrated Pedersen conductance (purple color scale), ordered by substorm phase along with contours of the FAC distribution at each phase. We overplot contours of upwards and downwards FAC distributions, colored dark red and teal respectively, at intervals of 0.10 μA m^{-2} from 0.05 μA m^{-2}. This figure is plotted for the example magnetic latitude substorm onset bin of 63°–65° degrees. In Figure 4, in a similar format as the previous figure and again for the example magnetic latitude substorm onset bin of 63°–65° degrees, we plot a set of differences image (purple-green color scale) showing the change in the conductance from the previous phase time step, expressed as a percentage. In these figures, the conductance begins to increase at onset at latitudes above 70° and in MLT sectors just after local midnight. By 0.5 δt, increases in conductance occur across many MLT and magnetic latitudes. Conductances begin to reduce at lower latitudes at 0.75 δt, before starting to reduce at higher latitudes from 1.00 δt. By 1.25 δt, that is, into the early part of the recovery phase, changes in conductance are seen at the edges of the main auroral oval. FAC contours show list change in position throughout the substorm.

In Figure 5 we plot average E_0 and Q by MLT sector for a selection of MLTs, r the course of a substorm, for both the variable δt binning (top row), and a fixed time grid (bottom row). We observe the largest parameter values in all cases for the MLT = 23 hr sector (≈4.3 keV, and ≈6.8 ergs cm^{-2} s^{-1}). The lowest peak values for each variable are found at the extreme east and west edges of the selected MLTs, which peak below 4 keV and below 4,ergs cm^{-2} s^{-1}. Almost all E_0 increase simultaneously after onset, with a slight delay to the east and west. The mean energy flux Q rises sharply at onset for the fixed time binning, for all MLT sectors, whereas this is somewhat smeared out for the δt based grid. Q in the MLT = 23 hr and MLT = 00 hr show a rapid reduction to levels similar to the other MLT sectors by 2 δt or by 1.5 hr after onset.

We now explore the behavior of various parameters over the course of an average substorm, at all substorm onset magnetic latitude bins. In Figure 6 we plot a set of time series with each step a multiple of δt as defined
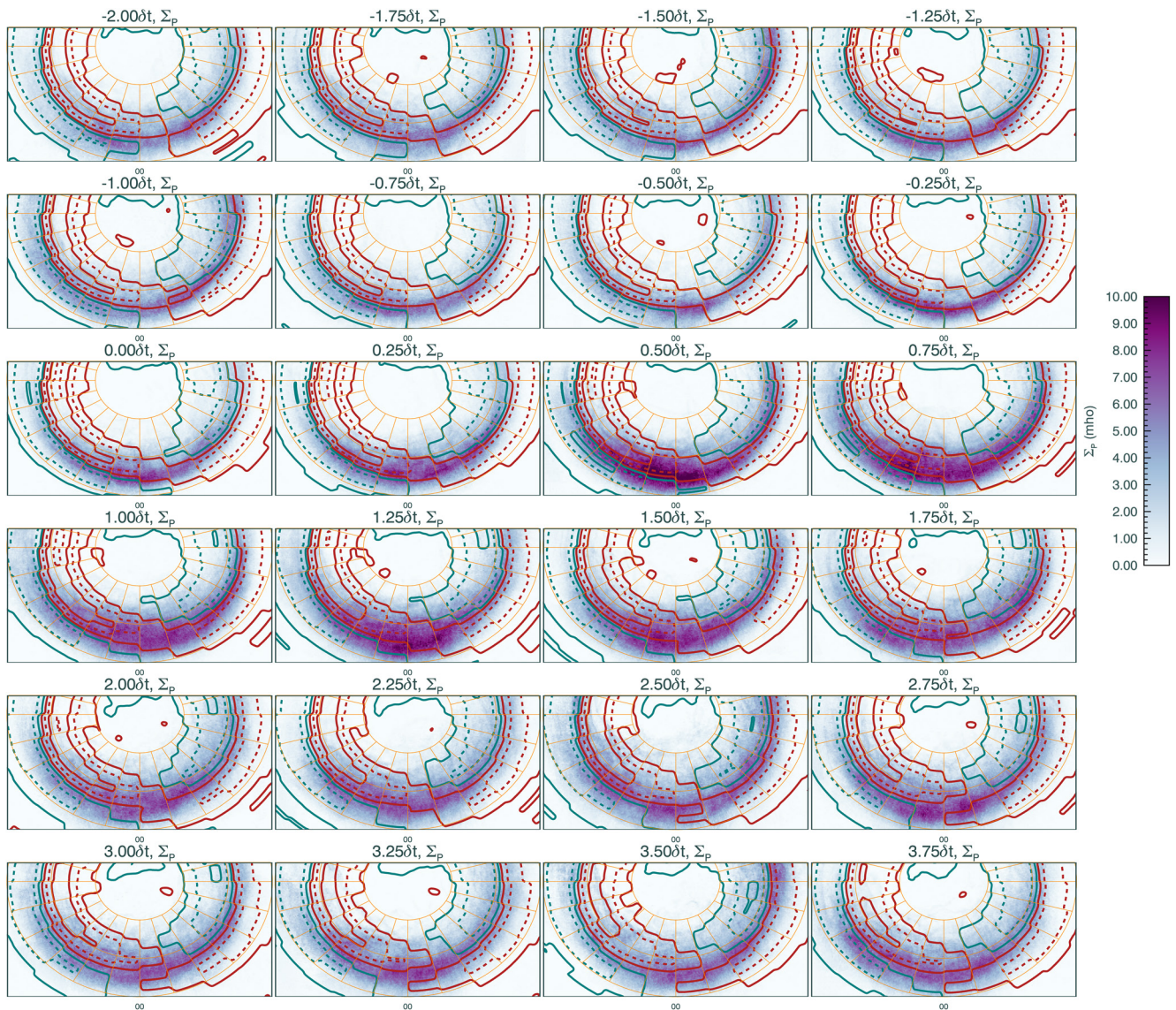
Figure 3. A series of images showing the nightside spatial distribution of height-integrated Pedersen conductance by substorm phase, for substorm onsets that occur between 63° and 65° degrees magnetic latitude. Each image is plotted on a magnetic-latitude, magnetic local time grid, with midnight to the bottom of each panel. On each panel we plot contours of the accompanying FAC distributions. Dark red contours are for upwards currents and teal contours are for downwards currents. Contours are plotted at intervals of 0.10 μA m^{-2} from 0.05 μA m^{-2}.

in Section 2. Each latitude bin is colored according to the legend given in the plot. Parameters from the SSUSI stacked data have been averaged over a wedge shape, within a MLT range of 21–02 hr and at co-latitudes less than 30° to encompass the auroral bulge. We plot a time series of the mean energy (E_0), energy flux (Q), and ratio between Q and E_0, the mean height-integrated derived Hall then Pedersen conductance, and then the mean Pedersen conductance offset from the mean conductance in the time period from $-2\,\delta t$ to $-0.5\,\delta t$, that is, prior to onset. We also plot the mean up and down FAC densities, taken from all contributing individual values in a given spatial wedge shape. These values are averaged over all latitudes, but taken in a narrow MLT sector between 4 and 5 hr MLT to encompass the maxima of the region 2 FACs in the post midnight sector. The spatial selection applied here extracts region 2 upwards FAC and region 1 downwards FAC.

In Figures 6a, 6b, 6d, and 6e, we observe that E_0, and Q, and the derived conductances are broadly ordered by magnetic latitude of onset. The peak parameter values are for the second to lowest magnetic latitude substorms occurring between 63° and 65°. The derived Hall and Pedersen conductances peak at nearly 11 mho and 5 mho, respectively, for the 63°–65° bin. All parameter values decrease with increasing magnetic latitude, although the
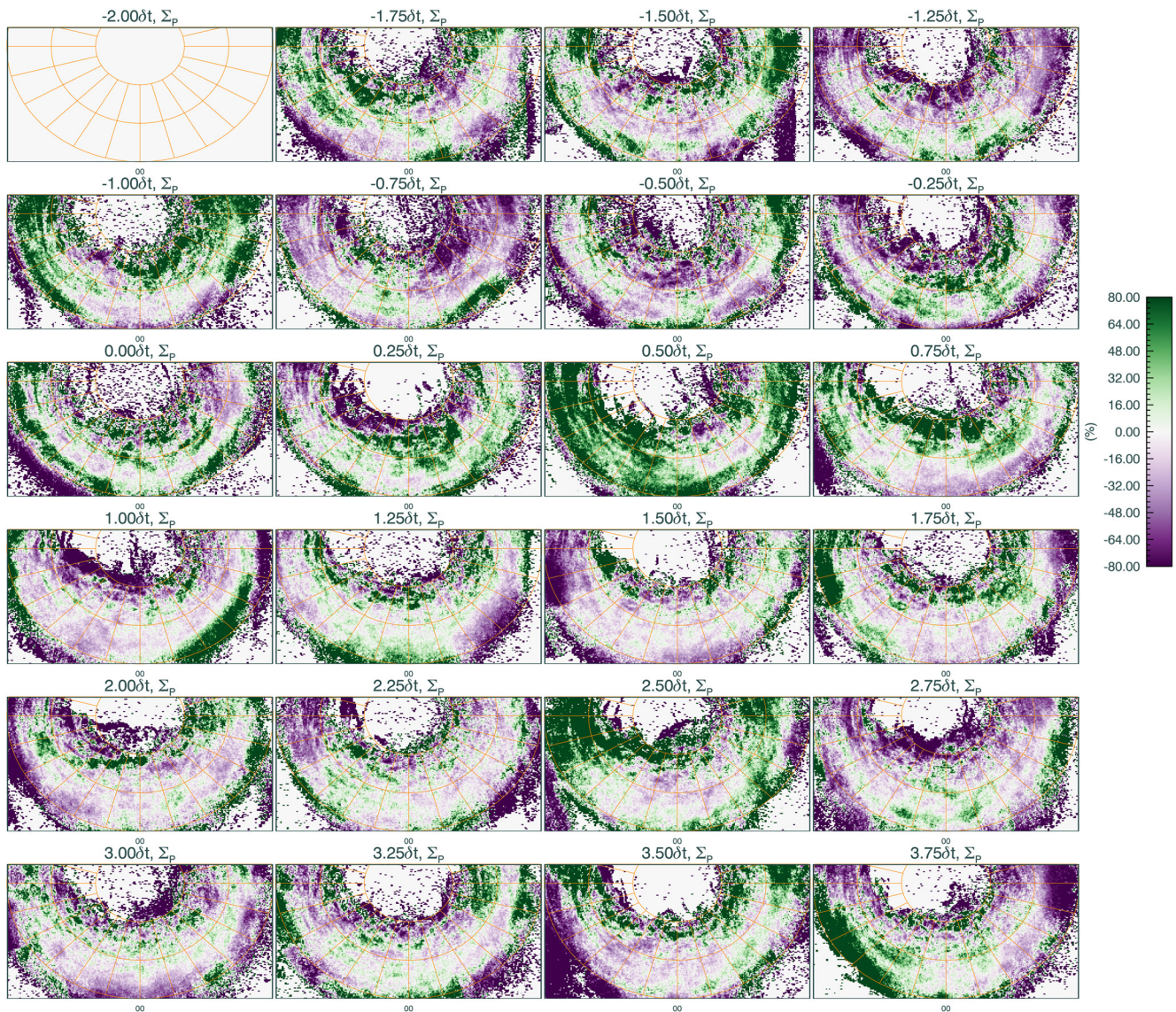
Figure 4. A series of images showing the percentage difference in Pedersen conductance from the previous normalized-time step, for substorm onsets that occur between 63° and 65° degrees magnetic latitude. The orientation and organization of the plots is as in Figure 3.

highest latitude bins over 71° are almost indistinct from one another. E_0 increases after onset, reaching a maximum of $\approx$3.5 keV within 1.25 δt after onset, with the exception of the lowest latitude substorms of 50°–63°, which is slower to ramp up and peaks at 1.75 δt at 3.2 keV. At the majority of these energies, the Gaussian assumption used in the SSUSI data set results in lower derived Pedersen conductances as compared to the Maxwellian assumption. An increase in Q is observed by 1 δt after onset, peaking at 4.3 ergs cm^{-2} s^{-1}. The 63°–65° substorms parameter values remain elevated after onset for the whole normalized-time period shown (4 δt). To a lesser extent, this slow delay in recovery to pre-substorm values is also seen in magnetic latitude bins 50°–63° and 65°–67°.

Figure 6c shows the mean ratio between Q and E_0 during a substorm. This ratio gives an indication of the number of precipitating particles. Most magnetic latitude bins, exhibit a slight rise in the ratio from substorm onset at about 1.3 erg cm^{-2} s^{-1} keV^{-1} to a maximum of 1.8 erg cm^{-2} s^{-1} keV^{-1}, an increase of approximately 40%, which lasts until approximately 1.25 δt interval post onset. The highest latitude bin, for onsets above 73°, only sees an increase 0.5δt after onset, but then shows a large variation in the ratio. Similarly, the lowest latitude bin 50° and 63°, shows large variations in the ratio from 1.75δt. Both these bins have the lowest number of contributing substorm onsets, and may show the largest variation in substorm duration. Given the flatter changes in E_0 as compared to Q, it appears that increases in mean energy flux Q at substorm onset is driving changes after the
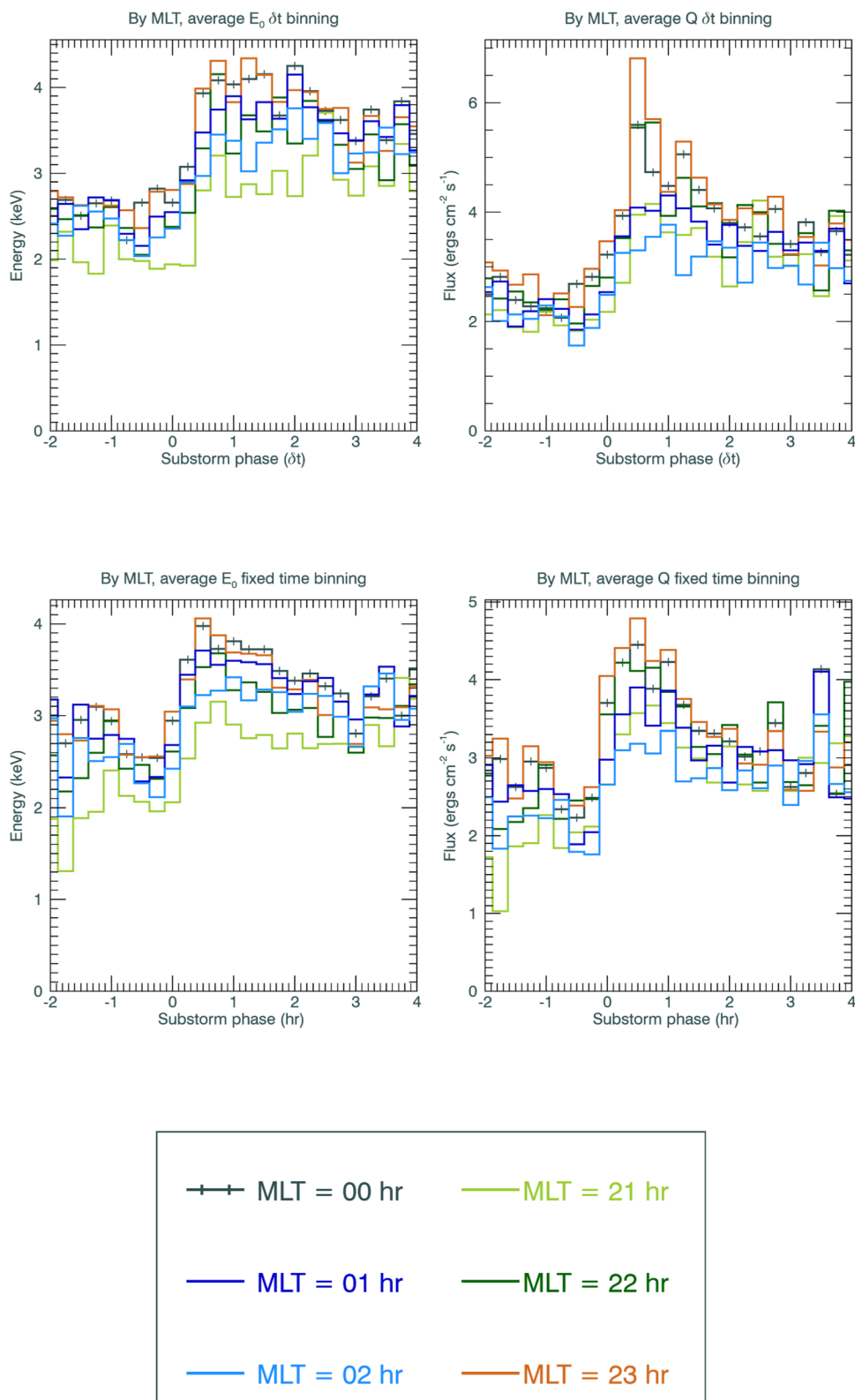
Figure 5. E_0 and Q over the course of a substorm by MLT, for substorms with onsets that occur between 63° and 65° degrees magnetic latitude. The top row is for the δt-defined time grid, and the bottom row for the fixed time binning.
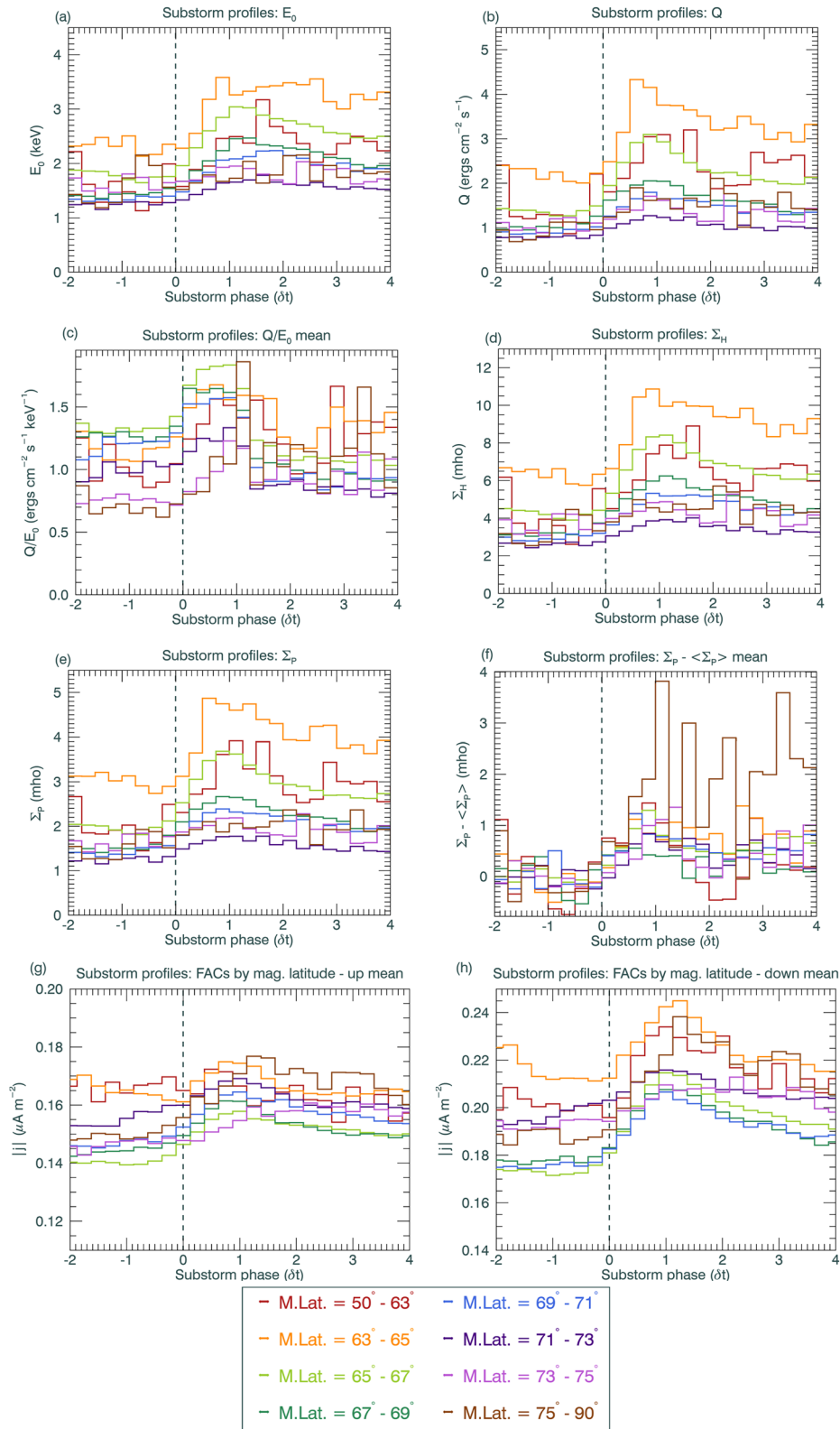
Figure 6.

recovery phase at 1 δt, rather than any marked difference in the mean energy of the precipitating particles. We explore this issue in our discussion below.

In Figure 6f, shows the Pedersen conductance offset from the average Pedersen conductance between 2 δt and 0.5 δt prior to onset. We include this plot as we are interested in changes to derived conductance values. This plot baselines each contributing substorm by reducing any biases in the data that may exist as the result of geomagnetic storms whereby large conductances prior to onset may influence our results. However, as we see no magnetic latitudinal dependence here, large geomagnetic storms do not appear to be causing any biases in the previous panels. The highest latitude bin over 75° shows elevated values above the mean after onset, and is likely to reflect weaker storms with a larger variety of durations.

In Figures 6g and 6h, the upwards FACs show less clear behavior over the course of a substorm than the downwards FACs. We note a slow increase in the magnitude of the average upwards current building up to a maximum at 1 δt, for the majority of the magnetic latitude bins. The largest current magnitudes are seen for the 63°–65° and 75°–90° magnetic latitude bin. One exception occurs for the lowest bin of onsets, from 50° to 63° which shows elevated average upwards current magnitudes prior to onset, which decrease after onset. Also, the bin from 73° to 75° shows a delayed and a very slow ramp up to the peak in the average upwards current magnitudes after more than 2 δt.

The downwards, or region 1, FACs, do show a clearer ordering by magnetic latitude into two regimes, with the exception of the highest latitude onsets above 75°. Those for the lowest latitude bins, ranging from 50° to 65° magnitudes show much large average downwards currents magnitudes than the other magnetic latitude bins, which in turn, show very little dependence on latitude above 65°. All magnetic latitude bins show an increase in current magnitude after onset, peaking in the main around 1 δt. The current magnitudes recover similarly, and slowly between latitude bins after onset.

In Figure 7 we show histograms of all the contributing or calculated values from the SSUSI and AMPERE data sets; for E_0, Q, Hall and Pedersen conductances, and the FACs split into up, red, and down, blue, currents. The FACs are given for the whole data set, regardless of substorm onset latitude. E_0 is limited to 20 keV through the SSUSI data processing procedures, and the distribution by energy is not dependent on the magnetic latitude of onset. The Q values show a separation by substorm onset magnetic latitude, whereby the 63°–65° magnetic latitude bin exhibits the highest values of Q, and across all Q this latitude bin has a larger number of contributing points.

In Figure 8 we plot a similar set of panels as for Figure 6, but instead of using the δt time step, calculated for each contributing substorm individually, we use a simple fixed time step of 0.25 hr to perform the superposed epoch analysis. The fixed binning time series in Figure 8 shows similar behavior to that based on δt in Figure 6. The magnetic latitude bin with the largest values of E_0 and Q at substorm onset is 63°–65°, as before for the δt grid. The lowest magnetic latitude bin, for 50°–63° is the most erratic. The large values at the beginning and end of the substorm period around 2 hr prior or beyond 3 hr after onset may indicate that after this time it is likely that a second substorm had occurred so that at the extremes of the time series overlapping substorms are being detected. The remaining bins are ordered by magnetic latitude, whereby the largest parameter values seen for the lowest magnetic latitude onsets, as seen previously. As before, parameters peak before 1 hr after onset. FAC magnitudes for these fixed bins are strongest for the lowest latitude bins, as seen previously, and again this is most apparent for the downwards (region 1) FACs. Here, the 63°–65° current magnitudes are largest by some margin, for both upwards and downwards FACs.

4. Discussion

Here we discuss the general progression of a substorm as observed in this work using a variable time and fixed time superposed epoch analysis, with regards to the mean energy and energy flux, and derived height-integrated conductances, and also in respect to changes observed in FAC morphology and magnitude. We also consider the magnetic latitude of the substorm onset.

Figure 6. Adjusted time series of various quantities versus the δt defined step of an average substorm, by magnetic latitude bin, averaged over a restricted 21–02 hr MLT sector and down to latitudes of 30°. Panels (a–c) E_0, then Q, and the ratio between them. Panels (d–f) derived Hall, and Pedersen mean height-integrated conductances, followed by the Pedersen conductance adjusted by the mean from 2 δt to 0.5 δt prior to onset. Panels (g, h): timeseries for average up, and then down field-aligned currents in a narrow MLT wedge, parameterized by magnetic latitude as the other parameters, over the course of an average substorm. A key to the color scheme is shown bottom right. Dashed vertical lines mark onset.
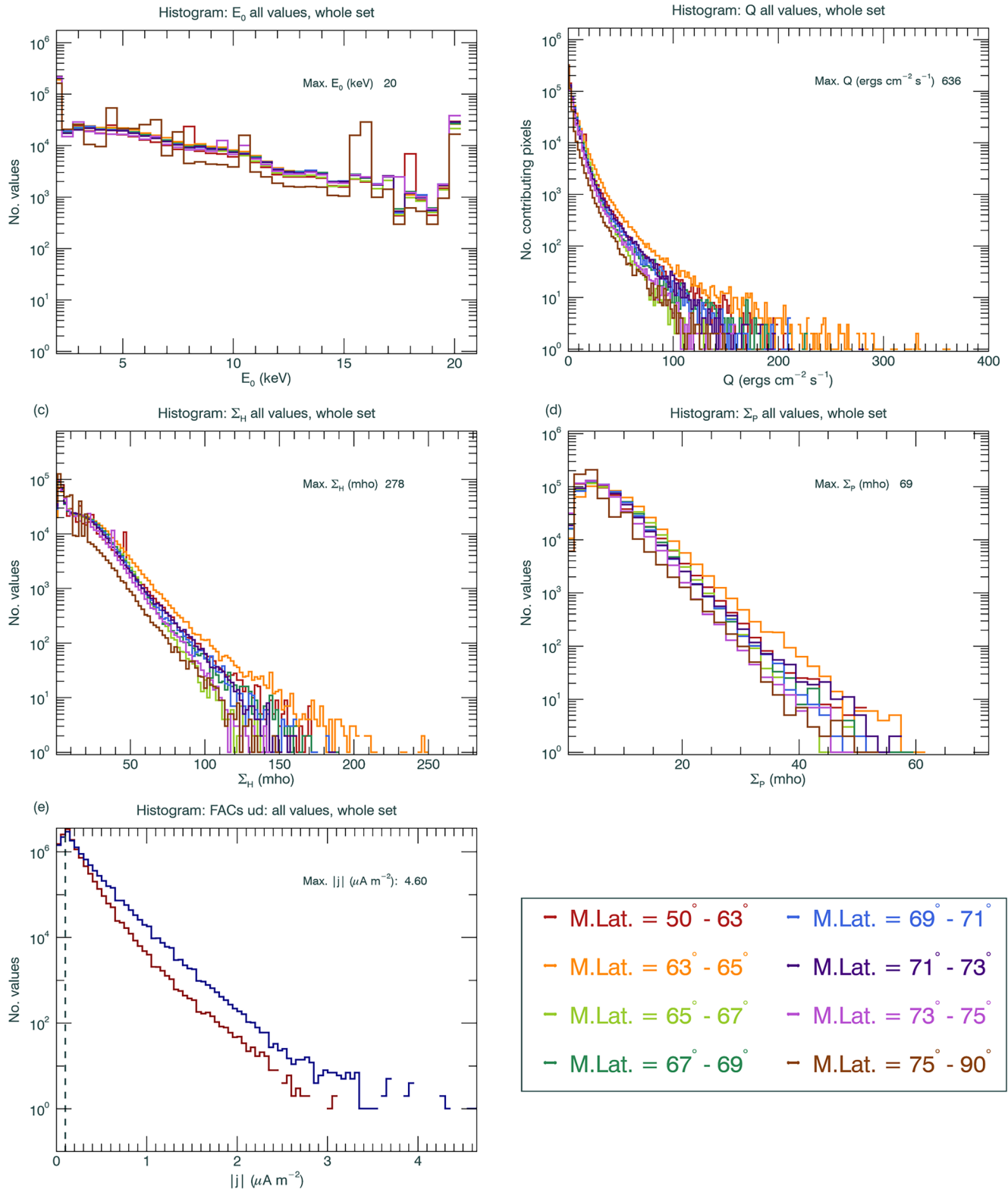
Figure 7. A set of histograms showing the distribution of all contributing data parameters for E_0, Q, and the derived Hall and Pedersen conductances, and the field-aligned currents split into up, red, and down, blue, currents. The Q panel has a restricted x-axis range to better show differences between magnetic latitude bins. The dashed line in (e) shows the threshold current density applied to the AMPERE data set.
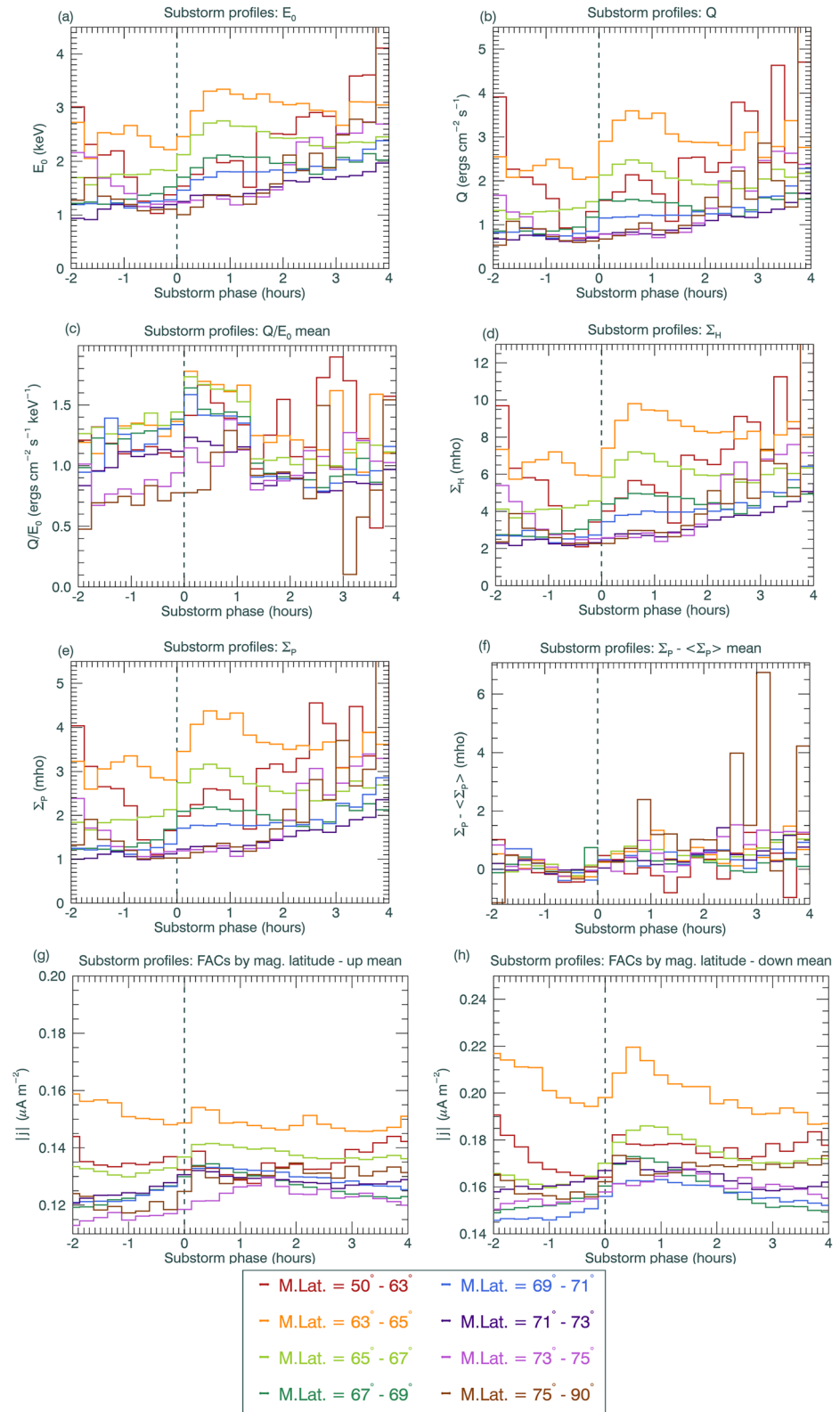
Figure 8. A set of time series in the same layout as Figure 6, but using a fixed time step of 0.25 hr for the superposed epoch analysis.

The progression of a substorm was explored via images of nightside conductances with overlaid contours of FACs, along with the difference between each variable time step in Figures 3 and 4. The sequence shown in these figures, for one example onset latitude bin, follows the well-support description of a substorm as outlined in Akasofu (1964). The conductances have been derived from the mean energy and mean energy flux parameters obtained via auroral emissions data taken by DMSP/SSUSI. During the recovery phase, at approximately 1.25 δt, large differences in conductance occurred at the edges of the main auroral oval. These changes suggest that dramatic differences in conductances in these regions may be due to rapid changes to the aurora or auroral oval such as pulsating aurora during the recovery phase, giving rise to the large percentage changes observed here. Pulsating aurora are most likely during the recovery phase of a substorm, with energies of ranging from a few to 100 keV, much exceeding those values in the diffuse aurora (Nishimura et al., 2020, and references therein). These pulsations are likely to exhibit dynamic energy flux variations as determined by correlations of their occurrence with variable particle fluxes measured at geosynchronous orbits (Lessard, 2012). Alternatively, the large changes in conductance could be due to artifacts of the averaging technique involving low numbers of contributing pixels, or less likely due to larger transient auroral events such as transpolar arcs which have not been screened for here. Clear evidence of increased conductance at onset was observed even when the magnetic latitude of substorm onset was not considered, as in Figure 5 of Carter et al. (2020).

Similar to the work in Carter et al. (2020), we explored the changes in E_0, Q, and derived height-induced conductances with respect to the MLT sector over the course of a substorm, in Figure 5. The lowest peak values for each variable are found at the extreme east and west edges of the selected MLTs, which is consistent with the previous work of others, for example, Walach et al. (2017). We do not observe a dawn-dusk asymmetry in the E_0, Q, which would imply an asymmetry in the Pedersen conductances as was found by Olifer et al. (2021), although the MLTs presented here are only those within 2 hr about midnight. Olifer et al. (2021) inferred increased electron precipitation to be the cause of increased conductances in the dawn sector, which is particularly noticeable following large substorms, whereas we have made no segregation based on substorm strength here and any asymmetry effect may be averaged out. We do not see a clear faster change in E_0 eastwards, toward MLT = 02 hr, as compared to a slower expansion westwards to MLT = 21 hr, as implied by the work of Gjerloev et al. (2007).

The progression of average parameters over the course of a substorm is explored in Figures 6 and 8, in panels (a) and (b) in both figures. Changes in E_0, and Q are largest and slower to recover for the lowest magnetic latitude bins, which is consistent with Grocott et al. (2009) and Milan et al. (2009) who showed that lower-latitude onset substorms, with onsets at magnetic latitudes less than 65°, produced brighter aurora that also persisted for longer. Following a detailed study of a substorm using precise but spatially constrained incoherent scatter radar measurements, Lester et al. (1996) inferred an increase in precipitating particle energy to more than 10 keV during the substorm recovery phase, or post 1 δt in comparison to the time series here, whereas they observed that the expansion phase mean energy remained fairly constant at approximately 2.5 keV. This was for one substorm, detected by a set of magnetometers between 63.6° and 67.3° magnetic latitude, and the mean energy here is slightly lower than 2 keV prior to onset for magnetic latitudes between 65° and 67°. Here, we see an increase in precipitating energy before the recovery phase starts at 1 δt, but a peak in energy after 1 δt to more modest mean energies up to a maximum of 3.6 keV, although here we average over a wide range of magnetic local times.

In Figures 6 and 8 panels (d) we check for biases due to precursor conditions in the magnetosphere by considering the offset in derived conductances after onset from those calculated prior to onset. The SOPHIE list uses the SuperMAG SML index in finding onsets. In the event of a large geomagnetic storm resulting in a long period decrease in the SML index, the SOPHIE technique is unlikely to find multiple instances of substorms occurring within an overall downward trend in SML. Substorms within lower-latitudinal ranges are likely to have a longer duration and show more intense auroral emissions (Milan et al., 2009).

Throughout this paper we have explored the progression of substorms with respect to the magnetic latitude of onset on both a variable and fixed time grid. The variable or fixed time ordered data behaved similarly, and the most important factor is the magnetic latitude of onset. Those onsets occurring between 63° and 65° magnetic latitude have exhibit differences in E0 and Q, as compared to other latitudes, in terms of substorm progression, as shown in Figure 6 and overall in contributing parameters as shown in Figure 7.

Milan et al. (2019, and references therein) explored convection braking for substorm with low-latitude onsets, and they quote a threshold of 65° magnetic latitude, above which convection braking is unlikely to occur. Onsets which start below 65° magnetic latitude are likely to have a more intense auroral response, leading to enhanced

conductance (e.g., in Figure 6 panel (e)) in the auroral bulge, which arrests the convection flow. We make no selection based on a minimum time between substorm onsets in our processing steps, and so our data set may include sawtooth events whereby a substorm-like signature is seen to repeat approximately every 3 hr (Borovsky et al., 1993), although these are rare phenomena occurring during enhanced geomagnetic activity (Walach & Milan, 2015).

The largest Q values were clear for substorms occurring between magnetic latitudes of 63°–65°, as shown in Figure 7. We postulate that enhanced conductances for these latitudes appear driven by increased flux, rather than an increase in the energy of precipitating particles. Individual Hall and Pedersen conductances, derived from measurements at individual pixels, can peak at over 200 mho or 60 mho respectively. The reason why this particular range of latitudes shows a different distribution of Q values forms the basis of an ongoing investigation. We have eliminated the case that one, spurious SSUSI observation has resulted in these large Q values, by inspecting the contributing observations within this latitudinal bin. Preferential detection of substorms within the SOPHIE set for example, due to favorable ground-conductivity at these latitudes needs to be investigated, although this particular latitudinal bin is not the most populated of all bins, as shown in Figure 1.

FAC contours show little change in position throughout the substorm, during the series presented in Figure 3. The technique employed here has smeared out the subtle approximately 1-degree latitudinal changes seen in FAC distributions in magnetic latitude, that are seen on a case to case basis during substorms (Coxon et al., 2014). However, evolution of the FACs over the course of a substorm is observed, and is apparent in the time series for both the variable and fixed time superposed epoch analysis, as explored in Figures 6 and 8. The FACs are also segregated by substorm onset magnetic latitude, with those occurring between 63° and 65° exhibiting the largest magnitude FACs. This is most apparent for the downward FACs. The upwards FAC in the narrow MLT sector used for the time series of Figures 6 and 8 represent region 2 FACs. A robust positive correlation between conductance and upwards FAC magnitude was observed by Robinson et al. (2020) between 03 and 06 hr MLT under dynamic geomagnetic storm-time conditions, showing the statistical relation between FACs and conductance in this MLT sector. Region 1, in this sector downwards FACs, have been shown to have higher current magnitudes compared to region 2 FACs by about 20% within 1 hr of onset on average (Coxon et al., 2014). We see in excess of 20% greater FAC current magnitude between region 2 (upwards) and region 1 (downwards) FACs here. FACs and Σ_P both peak within 1 δt after substorm onset, and recovery times are similar, regardless of latitude of onset. The fixed time grid shows a faster recover in FAC magnitude for the lowest latitude onsets as compared to the Σ_P values.

The normalization of the substorms to δt, defined as the duration of the expansion phase, that we used in this work may still hide features of the progression of a substorm. In this paper, we normalize the time series to multiples of δt. The modal δt value is shown in Figure 1 to between 0.10 and 0.20 hr, or 6–12 min Walach et al. (2017) made a statistical study of substorms using images of ultraviolet aurora, and saw the expansion phase typically lasting from 10 to 20 min after onset of the electron aurora, so therefore we justify the use of the independently calculated δt for binning of the conductances, derived from auroral data, in this paper. It is not necessarily the case that a longer total-duration substorm will have a longer expansion phase, nor is it true that conversely, shorter total-duration substorms have shorter expansion phases. The end of the recovery phase, when the auroral electrojet lower envelope boundary returns to a quiescent state and which would enable the calculation of the overall duration of each substorm, is not stored in the Forsyth et al. (2015) list. Walach et al. (2017) observed the recovery phase to occur by 50 min post onset for the electron aurora, which for a modal δt of 0.15 hr equates to 1.25 δt. We see a peak in parameter values starting before 1 δt, but a slow recovery to values prior to onset. Smearing of the data will inevitably occur over either the δt or fixed-time grid. Even so, the binning used in this paper is able to order the height-integrated conductances, E_0, Q, and region 1 downwards FACs by magnetic latitude of onset.

The dominance of high-parameter values for substorms with onsets that occur between 63° and 65° magnetic latitude is still to be determined. The influence of the ring current modulating tail reconnection and arresting substorm onset may play a part (Milan et al., 2021). We leave this to future investigation.

5. Conclusions

We have examined the behavior of mean energy, mean energy flux, and height-integrated conductances over the course of a substorm, using a superposed epoch analysis of auroral emissions derived parameters. We examined the behavior on both an artificial, normalized-time grid based on the duration of the expansion phase, and a fixed

time grid. Average substorm time series are found for a set separated by the magnetic latitude of substorm onset into broad bins of different widths between 50° to approximately 80°. For both normalized and fixed time grids, the maximum parameter values were observed for onsets that occur between 63° and 65° magnetic latitude. Why this latitude bin shows larger parameter values is currently under investigation and forms the basis of another study. Changes in the mean energy flux shortly after substorm onset are greater than changes in the mean energy of the precipitation. Higher magnetic latitude onsets exhibit lower values, throughout an entire substorm. For the normalized time binning, magnetic latitude onsets behave similarly over the course of a substorm, with values peaking by the start of the recovery phase, and decaying afterward. Lower latitude onset parameters decay slower to their pre-onset values than high latitude onsets. The fixed time binning series are likely to include several overlapping substorms, which affects the lowest magnetic latitude bin the most. FACs respond to a substorm in a similar manner to the auroral parameters, and this is most apparent in the downwards current magnitudes. FAC current magnitudes are also ordered by magnetic latitude, so that the lower magnitude latitude onsets exhibit the highest current magnitudes.

This work uses parameters derived from auroral emissions that are obtained by low-altitude spacecraft observing the ionosphere from above, with the advantage of observing large areas of the polar cap over short durations. Future work will involve comparing the wide-field aurora-derived SSUSI parameters with those obtained during conjunctions with incoherent radar data taken from ground-based facilities, ideally under a range of seasonal and geomagnetic conditions. This will allow verification of the derived conductances, albeit in a spatially constrained region, specifically from the SSUSI data products. A comparison with alternative methods of deriving height-integrated conductances will be beneficial.

Data Availability Statement

The DMSP/SSUSI file type EDR-AUR data were obtained from http://ssusi.jhuapl.edu (data version 0106, software version 7.0.0, calibration period version E0018). AMPERE data were obtained from http://ampere. jhuapl.edu. The AMPERE-derived region 1 region 2 FAC radii are stored at https://doi.org/10.25392/leicester. data.11294861.v1. SuperMAG data can be found via the portal at http://supermag.jhuapl.edu. The parameterized variable-time grid data are stored at https://doi.org/10.25392/leicester.data.21724028.

References

Akasofu, S. I. (1964). The development of the auroral substorm. *Planetary and Space Science*, *12*(4), 273–282. https://doi. org/10.1016/0032-0633(64)90151-5

Anderson, B. J., Korth, H., Waters, C. L., Green, D. L., Merkin, V. G., Barnes, R. J., & Dyrud, L. P. (2014). Development of large-scale Birkeland currents determined from the active magnetosphere and planetary electrodynamics response experiment. *Geophysical Research Letters*, *41*(9), 3017–3025. https://doi.org/10.1002/2014GL059941

Anderson, B. J., Takahashi, K., & Toth, B. A. (2000). Sensing global Birkeland currents with iridium® engineering magnetometer data. *Geophysical Research Letters*, *27*(24), 4045–4048. https://doi.org/10.1029/2000GL000094

Borovsky, J. E., Nemzek, R. J., & Belian, R. D. (1993). The occurrence rate of magnetospheric-substorm onsets: Random and periodic substorms. *Journal of Geophysical Research*, *98*(A3), 3807–3814. https://doi.org/10.1029/92JA02556

Carter, J. A., Milan, S. E., Paxton, L. J., Anderson, B. J., & Gjerloev, J. (2020). Height-integrated ionospheric conductances parameterized by interplanetary magnetic field and substorm phase. *Journal of Geophysical Research: Space Physics*, *125*(10), e2020JA028121. https://doi. org/10.1029/2020JA028121

Clausen, L. B. N., Baker, J. B. H., Ruohoniemi, J. M., Milan, S. E., & Anderson, B. J. (2012). Dynamics of the region 1 Birkeland current oval derived from the active magnetosphere and planetary electrodynamics response experiment (AMPERE). *Journal of Geophysical Research*, *117*(A6), 6233. https://doi.org/10.1029/2012JA017666

Coxon, J., Milan, S., Clausen, L., Anderson, B., & Korth, H. (2014). The magnitudes of the regions 1 and 2 birkeland currents observed by ampere and their role in solar wind-magnetosphere-ionosphere coupling. *Journal of Geophysical Research: Space Physics*, *119*(12), 9804–9815. https://doi.org/10.1002/2014ja020138

Denton, M. H., Borovsky, J. E., Stepanova, M., & Valdivia, J. A. (2016). Preface: Unsolved problems of magnetospheric physics. *Journal of Geophysical Research: Space Physics*, *121*(11), 10783–10785. https://doi.org/10.1002/2016JA023362

Forsyth, C., Rae, I. J., Coxon, J. C., Freeman, M. P., Jackman, C. M., Gjerloev, J., & Fazakerley, A. N. (2015). A new technique for determining substorm onsets and phases from indices of the electrojet (sophie). *Journal of Geophysical Research: Space Physics*, *120*(12), 10592–10606. https://doi.org/10.1002/2015JA021343

Gjerloev, J. W. (2012). The SuperMAG data processing technique. *Journal of Geophysical Research*, *117*(A9), A09213. https://doi.org/10. 1029/2012JA017683

Gjerloev, J. W., Hoffman, R. A., Sigwarth, J. B., & Frank, L. A. (2007). Statistical description of the bulge-type auroral substorm in the far ultra-violet. *Journal of Geophysical Research*, *112*(A7), A07213. https://doi.org/10.1029/2006JA012189

Grocott, A., Wild, J. A., Milan, S. E., & Yeoman, T. K. (2009). Superposed epoch analysis of the ionospheric convection evolution during substorms: Onset latitude dependence. *Annales Geophysicae*, *27*(2), 591–600. https://doi.org/10.5194/angeo-27-591-2009

Lam, M. M., Freeman, M. P., Jackman, C. M., Rae, I. J., Kalmoni, N. M. E., Sandhu, J. K., & Forsyth, C. (2019). How well can we estimate pedersen conductance from the THEMIS white-light all-sky cameras? *Journal of Geophysical Research: Space Physics*, *124*(4), 2920–2934. https://doi.org/10.1029/2018JA026067

Lessard, M. R. (2012). A review of pulsating aurora. In *Auroral phenomenology and magnetospheric processes: Earth and other planets* (pp. 55–68). American Geophysical Union (AGU). https://doi.org/10.1029/2011GM001187

Lester, M., Davies, J. A., & Virdi, S. (1996). High-latitude Hall and Pedersen conductances during substorm activity in the SUNDIAL-ATLAS campaign. *Journal of Geophysical Research*, *101*(A12), 26719–26728. https://doi.org/10.1029/96JA00979

Liemohn, M. W. (2020). The case for improving the robinson formulas. *Journal of Geophysical Research: Space Physics*, *125*(10), e2020JA028332. https://doi.org/10.1029/2020JA028332

McGranaghan, R., Knipp, D. J., Matsuo, T., Godinez, H., Redmon, R. J., Solomon, S. C., & Morley, S. K. (2015). Modes of high-latitude auroral conductance variability derived from dmsp energetic electron precipitation observations: Empirical orthogonal function analysis. *Journal of Geophysical Research: Space Physics*, *120*(12), 11013–11031. https://doi.org/10.1002/2015JA021828

Milan, S. E., Carter, J. A., Sangha, H., Bower, G. E., & Anderson, B. J. (2021). Magnetospheric flux throughput in the dungey cycle: Identification of convection state during 2010. *Journal of Geophysical Research: Space Physics*, *126*(2), e28437. https://doi.org/10.1029/2020JA028437

Milan, S. E., Carter, J. A., Sangha, H., Laundal, K. M., Østgaard, N., Tenfjord, P., et al. (2018). Timescales of dayside and nightside field-aligned current response to changes in solar wind-magnetosphere coupling. *Journal of Geophysical Research: Space Physics*, *123*(9), 7307–7319. https://doi.org/10.1029/2018JA025645

Milan, S. E., Grocott, A., Forsyth, C., Imber, S. M., Boakes, P. D., & Hubert, B. (2009). A superposed epoch analysis of auroral evolution during substorm growth, onset and recovery: Open magnetic flux control of substorm intensity. *Annales Geophysicae*, *27*(2), 659–668. https://doi.org/10.5194/angeo-27-659-2009

Milan, S. E., Walach, M.-T., Carter, J. A., Sangha, H., & Anderson, B. J. (2019). Substorm onset latitude and the steadiness of magnetospheric convection. *Journal of Geophysical Research: Space Physics*, *124*(3), 1738–1752. https://doi.org/10.1029/2018JA025969

Mukhopadhyay, A., Welling, D. T., Liemohn, M. W., Ridley, A. J., Chakraborty, S., & Anderson, B. J. (2020). Conductance model for extreme events: Impact of auroral conductance on space weather forecasts. *Space Weather*, *18*(11), e02551. https://doi.org/10.1029/2020SW002551

Newell, P. T., & Gjerloev, J. W. (2011). Evaluation of SuperMAG auroral electrojet indices as indicators of substorms and auroral power. *Journal of Geophysical Research*, *116*(A15), 12211. https://doi.org/10.1029/2011JA016779

Nishimura, Y., Lessard, M. R., Katoh, Y., Miyoshi, Y., Grono, E., Partamies, N., et al. (2020). Diffuse and pulsating aurora. *Space Science Reviews*, *216*(1), 4. https://doi.org/10.1007/s11214-019-0629-3

Olifer, L., Feltman, C., Ghaffari, R., Henderson, S., Huyghebaert, D., Burchill, J., et al. (2021). Swarm observations of dawn/dusk asymmetries between Pedersen conductance in upward and downward field-aligned current regions. *Earth and Space Science*, *8*(7), e2020EA001167. https://doi.org/10.1029/2020EA001167

Paxton, L. J., & Anderson, D. E. (1992). *Far ultraviolet remote sensing of Venus and Mars* (Vol. 66, pp. 113–189). Washington DC American Geophysical Union Geophysical Monograph Series. https://doi.org/10.1029/GM066p0113

Paxton, L. J., & Zhang, Y. (2016). Far ultraviolet imaging of the aurora. In *Space weather fundamentals*. CRC Press.

Robinson, R. M., Kaeppler, S. R., Zanetti, L., Anderson, B., Vines, S. K., Korth, H., & Fitzmaurice, A. (2020). Statistical relations between auroral electrical conductances and field-aligned currents at high latitudes. *Journal of Geophysical Research: Space Physics*, *125*(7), e2020JA028008. https://doi.org/10.1029/2020JA028008

Robinson, R. M., Vondrak, R. R., Miller, K., Dabbs, T., & Hardy, D. (1987). On calculating ionospheric conductances from the flux and energy of precipitating electrons. *Journal of Geophysical Research*, *92*(A3), 2565–2569. https://doi.org/10.1029/JA092iA03p02565

Walach, M. T., & Milan, S. E. (2015). Are steady magnetospheric convection events prolonged substorms? *Journal of Geophysical Research: Space Physics*, *120*(3), 1751–1758. https://doi.org/10.1002/2014JA020631

Walach, M.-T., Milan, S. E., Murphy, K. R., Carter, J. A., Hubert, B. A., & Grocott, A. (2017). Comparative study of large-scale auroral signatures of substorms, steady magnetospheric convection events, and sawtooth events. *Journal of Geophysical Research: Space Physics*, *122*(6), 6357–6373. https://doi.org/10.1002/2017JA023991

Waters, C. L., Anderson, B. J., & Liou, K. (2001). Estimation of global field aligned currents using the iridium® system magnetometer data. *Geophysical Research Letters*, *28*(11), 2165–2168. https://doi.org/10.1029/2000GL012725